Article

The Energy Dissipation Mechanism and Damage Constitutive Model of Roof–CPB–Floor (RCF) Layered Composite Materials

Jie Wang [1,2,*], **Chi Zhang** [1,2,*], **Jianxin Fu** [1,2], **Weidong Song** [1,2] and **Yongfang Zhang** [1,2]

1   School of Civil and Resources Engineering, University of Science and Technology Beijing, Beijing 100083, China; fjx@ustb.edu.cn (J.F.); songwd@ustb.edu.cn (W.S.); b1903098@ustb.edu.cn (Y.Z.)
2   State Key Laboratory of High-Efficient Mining and Safety of Metal Mines of Ministry of Education, University of Science and Technology Beijing, Beijing 100083, China
*   Correspondence: wangjie123@ustb.edu.cn (J.W.); d202110040@xs.ustb.edu.cn (C.Z.)

Abstract: The stability of composite material that is composed of roof rock, cemented paste backfill (CPB), and floor rock has an important impact on safe mining within metal mines. In order to explore the mechanical properties, acoustic emission (AE), energy dissipation, and damage evolution of roof–CPB–floor (RCF) layered composite materials, uniaxial compression (loading rate 0.02 mm/min) AE tests on RCF materials with different CPB height ratios were performed. The test results show that: (1) the uniaxial compressive strength (UCS) and elastic modulus (E_R) of the RCF material were lower than those of the roof or floor rock and higher than that of the CPB. With the increase in the CPB's height ratio from 0.2 to 0.7, the (UCS and the E_R decreased from 18.42 MPa to 10.08 MPa and 3.15 GPa to 1.79 GPa, respectively, and the peak strain first decreased from 0.695 to 0.510 and then increased from 0.510 to 0.595. The (UCS increased as a polynomial function with the increase in the E_R. (2) The AE ring count first increased slowly, then increased rapidly, and finally maintained a high-speed increase. The AE cumulative ring count at the peak point decreased with the increase in the CPB height ratio. The energy dissipation showed that the elastic energy U_E accumulated slowly at first, then the dissipated energy U_D increased, and finally the U_E decreased and the U_D increased almost linearly. The U_T, U_E, U_D, U_E–U_T ratio and U_D–U_T ratio showed a decreasing trend, and the U_E–U_D ratio showed an increasing trend at the peak point with the increase in the CPB height ratio. (3) Two damage constitutive models were established based on the AE ring count and energy principle. The damage evolution process of RCF materials can be divided into three stages: the slow damage accumulation stage, stable damage growth stage, and rapid damage accumulation stage.

Keywords: RCF layered composite material (RCF); mechanical properties; acoustic emission (AE); energy dissipation; damage constitutive model

1. Introduction

Affected by the causes of its formation, the spatial shape of a gold ore body is usually complex, the dip angle of the ore body is usually small and approximately horizontal in its distribution, the thickness of the ore body is small, the thickness distribution is very uneven, and the surrounding rock is usually very broken [1–3]. Therefore, gold ore bodies are usually mined by the upward horizontal drift filling method. The rooms and pillars are arranged at intervals. First, the room is mined, then the goaf is filled with the tailings, and then the adjacent pillars are mined. In the process of pillar mining, the adjacent sides of the pillar are filled with cemented paste backfill (CPB), which forms a layered composite material with the roof and floor rock in order to bear pressure together to support the goaf and prevent the goaf from collapsing, so as to ensure the safety of the pillar mining [4–6]. In this situation, the overall stability of the layered composite material that is composed of roof rock, CPB, and floor rock is related to the safe mining and sustainable development of the mine. In addition, in the mining process, the thickness of the ore body will continue

to change, so the CPB height of the layered composite material will also vary with the different mining areas. Therefore, it is of great theoretical and practical significance to study the influence of the CPB height on the overall stability of layered composite materials.

Recently, domestic and foreign scholars have conducted in-depth research on the common pressure bearing mechanism of backfill and rock composite structures by means of an indoor test, theoretical research, and numerical simulation and they have achieved fruitful research results [7–12], which provide a lot of reference basis for the research of this paper. Wang et al. [13] studied the effects of roughness and the inclination of a nonlinear interface on the strength and failure of the backfill–rock combination under uniaxial compression. He et al. [14] carried out a uniaxial compression test on a CPB–rock combination, discussed the influence of various CPB cement tailings ratios on the mechanical properties of the CPB–rock combination, and analyzed the crack evolution law with the help of fractal theory. Wu et al. [15] analyzed the influence of the interface angle on the shear strength and deformation behavior of a backfill–rock combination under triaxial compression. Fang et al. [16,17] studied the shear characteristics of the rock–backfill interface with the help of a chemo–elastic coupling cohesive zone model. Yu et al. [18] investigated the effects of the rock–backfill volume fraction and confining pressure on the strength characteristics and failure modes of the rock–backfill combination model with the help of a triaxial compression test and CT scanning. Zhao et al. [19] used the Karagozian–Case concrete (KCC) model to analyze the uniaxial compressive mechanical behavior of the backfill–rock composite structure. However, through the above reference analysis, almost all of the studies on the backfill–rock combination structure focus on the two-body model. In the actual filling mining process, the CPB usually forms a three-body composite structure with the roof rock and floor rock in order for the three elements to bear the pressure together. There are great differences in the mechanical properties and deformation behaviors between the three-body composite structure, the single structure, and the two-body composite structure. Only studying the single structure or the two-body composite structure cannot fully characterize the actual situation. Therefore, it is necessary to study the mechanical properties of a roof rock–CPB–floor rock (RCF) layered composite material.

Furthermore, with the popularization and application of acoustic emission (AE) technology, more and more scholars use AE technology to study the evolution law of the AE parameters of rock, backfill, and other materials in the compression process, so as to analyze the evolution process of internal damage in materials [20–24]. Wang et al. [25] carried out a uniaxial compression AE test on three-layered cemented paste backfill, discussed the evolution law of the AE ring count, energy count, and amplitude during loading, and analyzed the temporal and spatial evolution law of cracks during loading with the help of AE positioning technology. Cheng et al. [26] utilized laboratory testing and PFC numerical simulation and analyzed the temporal and spatial evolution law of AE events under the uniaxial compression of cemented tailings backfill (CTB). Zhou et al. [27] carried out uniaxial compression and Brazilian splitting AE tests on CPB and studied the relationships between the AE fractal dimension, energy dissipation, and damage variables. Zhao et al. [28] investigated the correlation between the AE fractal dimension and mechanical damage of cemented tailings backfill with different cement–sand ratios. Wang et al. [29] studied the influence of joint inclination on the dynamic evolution law of rock cracks with the help of AE acoustic emission positioning technology. In summary, these scholars have derived fruitful research results regarding the AE characteristics of backfill and rock; however, there are relatively few studies on the AE characteristics of the rock and backfill combined structure, which has a wide research prospect.

In addition, whether it is filling material or rock material, the process of internal crack initiation, propagation, and penetration under a load is the process of the continuous conversion of internal energy. The energy absorption and storage characteristics of the filling materials determine their strength characteristics and failure modes [30–34]. Hou et al. [35,36] revealed the relationship between the internal energy evolution and stress development of the CPB during the whole loading process. Qiu et al. [37] elaborated the AE

energy dissipation characteristics of the CPB under uniaxial compression with the help of AE monitoring means. Xin et al. [38] studied the internal relationship between the internal compression energy, tensile energy, and waste rock content.

As many studies have analyzed the AE and internal energy evolution mechanism of filling materials by different means and from different angles, they have revealed the internal relationship between the damage, failure, and energy dissipation of filling materials. However, the above research objects were single medium materials or dual medium materials, which are characterized by a relatively uniform internal structure. Therefore, under the action of a load, their AE and internal energy distribution are also relatively uniform, and the relationship between their AE and energy dissipation is relatively simple [39]. The AE and energy consumption mechanism of rock–CPB–rock composite material are completely different from those of single-medium materials and dual-medium materials [40]. Firstly, there are more factors affecting the energy evolution of composite materials (rock properties, CPB properties, structural plane properties, etc.) [41,42]. Secondly, the internal structure of the composite materials is asymmetric and non-uniform and the stress distribution and deformation characteristics are more complex, resulting in very complex AE and energy evolution [10]. Finally, the composite materials have non-uniform structural planes and the energy transfer relationship between them is more complex and changeable [43]. Therefore, the AE and energy evolution of rock–CPB–rock composite materials need to be deeply studied.

The process of the gradual instability and failure of rock, backfill, and other materials under load is essentially a process of the continuous accumulation of internal damage [44]. Mastering the damage evolution process of rock and backfill is very important for its overall stability control. Wang et al. [45] constructed the damage constitutive model of rock-encased backfill with the help of the energy principle. Fu et al. [46] constructed the damage constitutive model of layered cemented tailings backfill considering its layered structure and analyzed the effects of layer numbers and the confining pressure on the damage evolution law. Liu et al. [47] constructed the damage constitutive model of cemented coal gangue–fly ash backfill and discussed the influence of curing temperature on damage evolution. Hou et al. [48] established a triaxial creep damage constitutive model of cemented gangue–fly ash backfill and analyzed its creep damage characteristics. Lin et al. [49] deduced the fatigue constitutive model of yellow sandstone based on the macro–micro coupled damage.

Consequently, the present AE detection and uniaxial compression experiments were carried out on RCF samples with the CPB height ratio of 0.2, 0.3, 0.4, 0.5, 0.6, and 0.7, respectively. Firstly, the (*UCS*, elastic modulus, and peak strain of each of the RCF samples were studied. The relationships between the (*UCS*, elastic modulus, and CPB height ratio, and the (*UCS* and elastic modulus were characterized. Secondly, the AE ring count characteristic and energy dissipation mechanism of the RCF samples with different CPB height ratios are analyzed. Finally, two damage constitutive models of the RCF materials have been established based on the AE and energy principle, and its damage evolution law is deeply discussed.

2. Materials and Methods

2.1. Research Background

The background of this present research is the Xinhui gold mine in Shandong Province, China. The length of the ore body is about 270 m, the thickness of the ore body in the gold mine in Shandong is 1–2.5 m, the dip angle of the ore body is about 20°, and the grade is about 3.15 g/t. The ore body is moderately stable and the stability of the hanging wall rock is poor. An upward horizontal drift filling mining method was adopted and the ore rooms and ore pillars were mined step by step. In the first step, the ore room is mined and the ore room goaf is filled with cemented paste backfill (CPB). In the second step, the ore pillar is mined. In the process of pillar mining, the CPB, roof rock, and floor rock form a layered composite material in order to bear the pressure together, so as to ensure the safety

of the pillar mining. Due to the uneven thickness of the ore body, the height ratio of the layered composite material is in dynamic change. The actual model and laboratory model of the roof rock–CPB–floor rock (RCF) layered composite materials are shown in Figure 1. The stability of the RCF layered composite material has an important impact on two-step pillar mining, so it is of great theoretical and practical significance to study its mechanical properties and damage evolution.
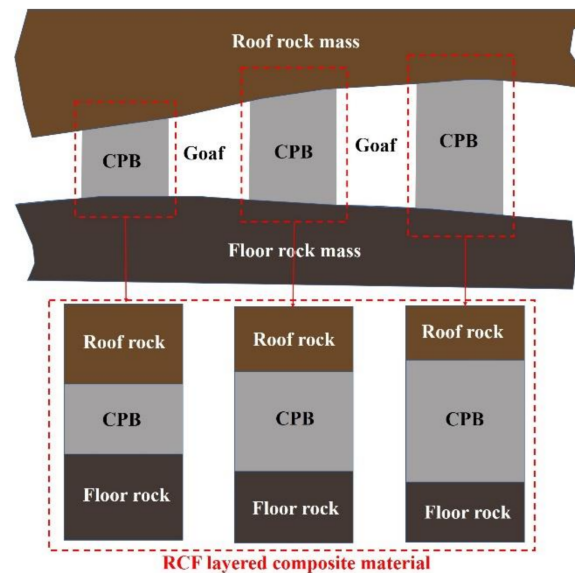

Figure 1. Layered composite material in mining field and laboratory of roof rock–CPB–floor rock (RCF).

2.2. Experimental Materials and Characteristics

The roof rock (Phyllite) that was used in the test came from the roof rock mass of the gold mine, as shown in Figure 2a. The floor rock (Hematite) that was used in the test came from the floor rock mass of the gold mine, as shown in Figure 2b. The tailings that were used in the test were from the full tailings of the mine. The cement that was used in the test was ordinary Portland cement (OPC) 42.5R. The water that was used in the test was laboratory tap water. The particle size distribution (PSD) curves of the full tailings and OPC are shown in Figure 3. The chemical compositions of the full tailings and OPC are shown in Table 1.
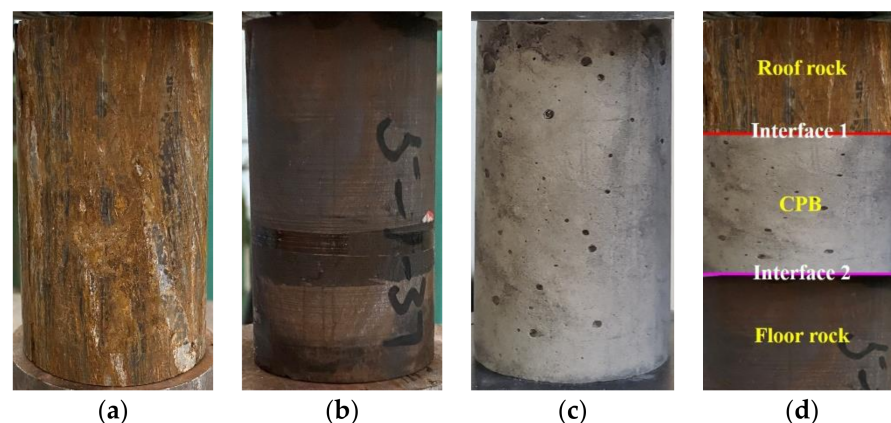

(**a**) (**b**) (**c**) (**d**)

Figure 2. Test samples: (**a**) Roof rock sample; (**b**) Floor rock sample; (**c**) CPB sample; (**d**) RCF sample.
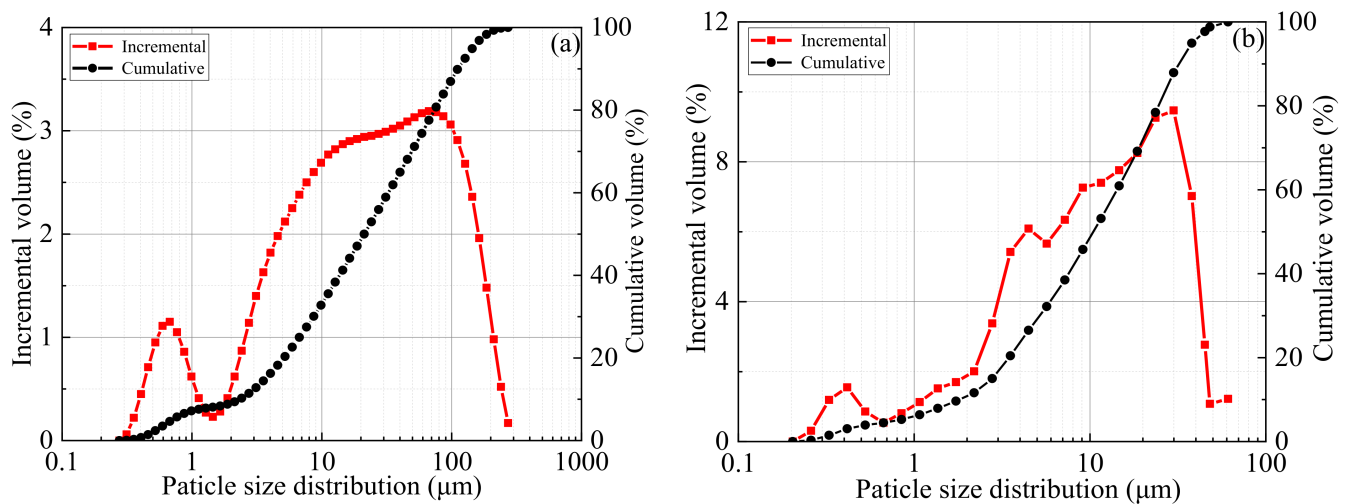
Figure 3. The PSD curves: (**a**) full tailings; (**b**) OPC.

Table 1. Chemical composition of the raw materials.

Sample	SiO$_2$	K$_2$O	CaO	P$_2$O$_5$	MgO	Al$_2$O$_3$	Fe$_2$O$_3$	SO$_3$
OPC (%)	20.10	0.37	61.8	/	1.57	5.11	2.91	1.98
Full tailing (%)	66.95	4.40	7.68	0.15	2.24	11.71	4.91	0.20

2.3. Sample Preparation

Four types of samples were prepared: (1) the intact roof rock sample (Figure 2a); (2) the intact floor rock sample (Figure 2b); (3) the intact CPB sample (Figure 2c) (the cement-to-tailings ratio of which was 1:4, the slurry concentration of which was 75%, and the curing age of which was 28 days); (4) the RCF layered composite material sample (Figure 2d). The overall size of the four types of samples was the same, with a diameter of Φ = 50 mm and a height of H = 100 mm. The height of the CPB in the middle of the RCF sample was set at 20, 30, 40, 50, 60, and 70 mm and the heights of the roof rock and floor rock were the same, which were set at 40, 35, 30, 25, 20, and 15 mm, respectively. The manufacturing process of the RCF sample was executed as follows: First, the prepared intact CPB sample and rock sample were cut according to the specified height. Then, the tailing slurry with the cement-to-tailings ratio of 1:4 and slurry concentration of 75% was prepared. Finally, the prepared slurry was used to paste the cut roof rock, CPB, and floor rock together to form an RCF sample with a total height of 100 mm. The sample design scheme and mechanical parameters are shown in Tables 2 and 3.

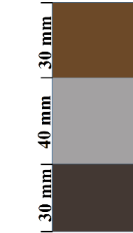**Table 2.** Mechanical parameters and number of intact samples.
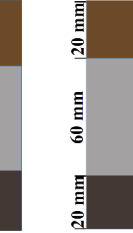
Intact Sample	Sample No.	(*UCS* (MPa)	Elastic Modulus (GPa)	Peak Strain (%)
Roof rock	RR	23.91	4.13	0.71
Cemented paste backfill	CPB	7.25	1.65	0.57
Floor rock	FR	41.00	5.64	0.92

2.4. Uniaxial Compression AE Test

A GAW-2000rock mechanics testing machine made by Chaoyang Test Instrument Co., Ltd (Changchun, China) was used to carry out a uniaxial compression test. The loading mode was set to displacement control and the loading rate was 0.5 mm/min. During the loading process, the computer system recorded the displacement and load of the testing machine in real-time. After the loading, the size parameters of the sample were input into the system

and the system automatically calculated the strain and strain value of the sample throughout the whole loading process. At the same time, the peak stress, peak strain, and other parameters of the sample were also recorded. After the test, the data file was exported and could then be used in the various required formats. For the whole process of uniaxial compression, PCI-2 AE equipment made by Physical Acoustics Co., Ltd (Princeton, NJ, USA) was used for the AE signal acquisition. The frequency of the AE sensor was 140 kHz and the noise threshold was set to 45 dB.

Table 3. Mechanical parameters and number of RCF samples.

CPB Height (h/H) Ratio	0.2	0.3	0.4	0.5	0.6	0.7
Sample No.	RCF2	RCF3	RCF4	RCF5	RCF6	RCF7
RCF samples models						
(UCS (MPa)	18.42	13.54	10.69	10.35	10.28	10.18
EM (GPa)	3.15	2.74	2.44	2.16	1.96	1.79
Peak strain (%)	0.695	0.567	0.514	0.510	0.542	0.595

3. Results and Analysis

3.1. Mechanical Properties of RCF Materials

The mechanical properties of the RCF layered composite materials are related to the safety and stability of the goaf roof. As can be seen from Table 1, the uniaxial compressive strength ((UCS) and elastic modulus (E_R) of the floor rock were the largest, followed by those of the roof rock, and then by those of the (UCS and E_R of the cemented paste backfill (CPB), which were the smallest. As can be seen from Table 2, the (UCS and E_R of the RCF material decreased with the increase in the height (h/H) ratio of the middle CPB and the (UCS and E_R of the RCF material were less than those of the roof rock and floor rock, but greater than those of the CPB.

3.1.1. Uniaxial Compressive Strength

Figure 4 shows the relationships between the (UCS' (The normalized value of uniaxial compressive strength), (UCS ratio, and CPB height (h/H) ratio. As can be seen from Figure 4a, the (UCS' of the RCF material decreased with the increase in the CPB height ratio. When the CPB height ratio increased from 0.2 to 0.7, the (UCS' of the RCF material decreased from 1 to 0.41, 0.06, 0.02, 0.01, and 0. With the increase in the CPB height ratio of the RCF material, the proportion of the CPB's weak sandwich increased. Under the action of the load, the overall bearing capacity decreased and the (UCS' decreased. An exponential function can be used to characterize the relationship between the (UCS' of the RCF material and the CPB height ratio:

$$(UCS' = -0.02 + 7.29 \times \exp[-9.77 \times (h/H)] \tag{1}$$

where (UCS' is the normalized value of uniaxial compressive strength of the RCF material and h/H is the CPB height ratio.
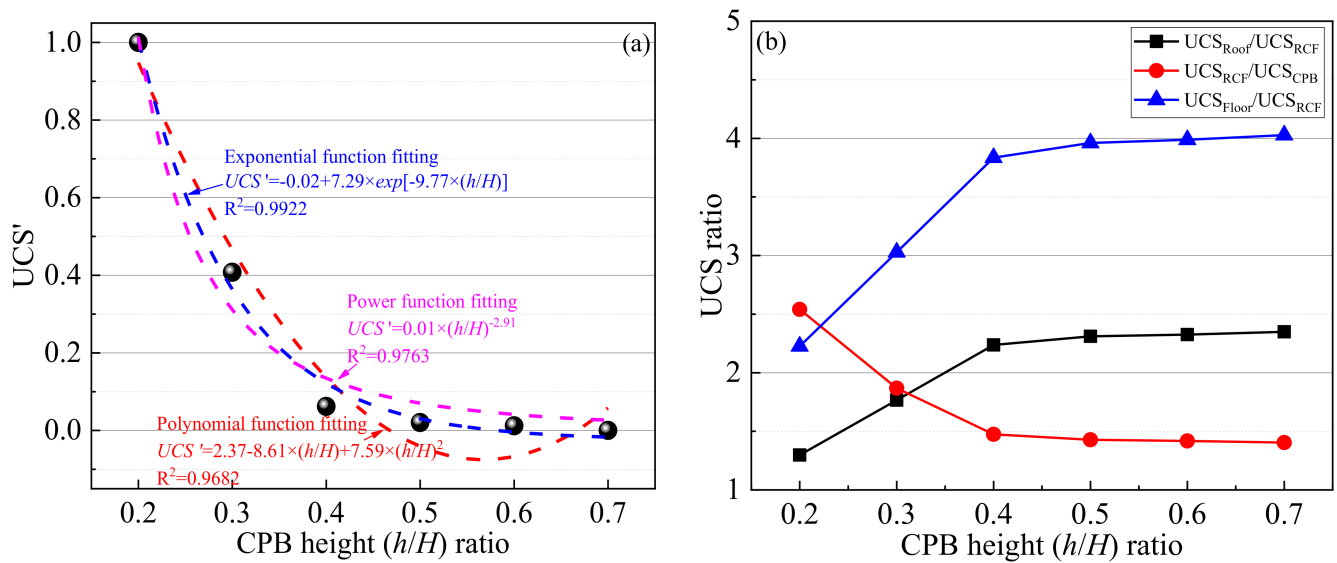
Figure 4. (*UCS* of RCF material: (**a**) (*UCS* and h/H ratio of RCF material; (**b**) (*UCS* ratio and h/H ratio.

The (*UCS* ratios of the roof rock (RR) and floor rock (FR) to the RCF material represents the (*UCS* deterioration degree of the RCF material on the RR and FR, respectively. The (*UCS* ratio of the RCF material to CPB represents the (*UCS* strengthening degree of the RCF material on the CPB. Figure 4b shows that the (*UCS*$_{Roof}$–(*UCS*$_{RCF}$ ratio and the (*UCS*$_{Floor}$–(*UCS*$_{RCF}$ ratio increased with the increase in the CPB height ratio. When the CPB height ratio increased from 0.2 to 0.7, the (*UCS*$_{Roof}$–(*UCS*$_{RCF}$ ratio increased from 1.298 to 2.349 and the (*UCS*$_{Floor}$–(*UCS*$_{RCF}$ ratio increased from 2.226 to 4.028. In addition, the (*UCS*$_{RCF}$–(*UCS*$_{CPB}$ ratio decreased with the increase in the CPB height ratio. When the CPB height ratio increased from 0.2 to 0.7, the (*UCS*$_{RCF}$–(*UCS*$_{CPB}$ ratio decreased from 2.541 to 1.404. When the CPB height ratio was greater than 0.4, the strength of the RCF material approached the strength of the CPB, the change rate of the RCF material's strength decreased, and the influence of the CPB height ratio on the RCF material's strength decreased significantly. This is because the height of the CPB layer began to be greater than that of the roof rock or floor rock layers when the CPB height ratio was greater than 0.4. the CPB, as the weak structure, began to be the main part of the RCF material and the failure of the CPB layer can be seen to be the decisive factor for the failure of the RCF structure. Therefore, the change of the RCF material's strength decreased significantly and was close to zero when the CPB height ratio was greater than 0.4.

3.1.2. Elastic Modulus

Figure 5 shows the relationship between the $E_R{}'$(The normalized value of elastic modulus), E_R ratio of the RCF material, and the CPB height ratio. As can be seen from Figure 5a, the $E_R{}'$ of the RCF material decreased with the increase in the CPB height ratio. When the CPB height ratio increased from 0.2 to 0.7, the $E_R{}'$ of the RCF material decreased from 1 to 0. With the increase in the CPB height ratio, the proportion of the CPB's weak sandwich increased, resulting in a decrease in the overall stiffness of the RCF samples. In addition, a polynomial function can be used to characterize the relationship between the $E_R{}'$ of the RCF material and the CPB height ratio:

$$E_R{}' = 1.68 - 3.87 \times (h/H) + 2.10 \times (h/H)^2 \tag{2}$$

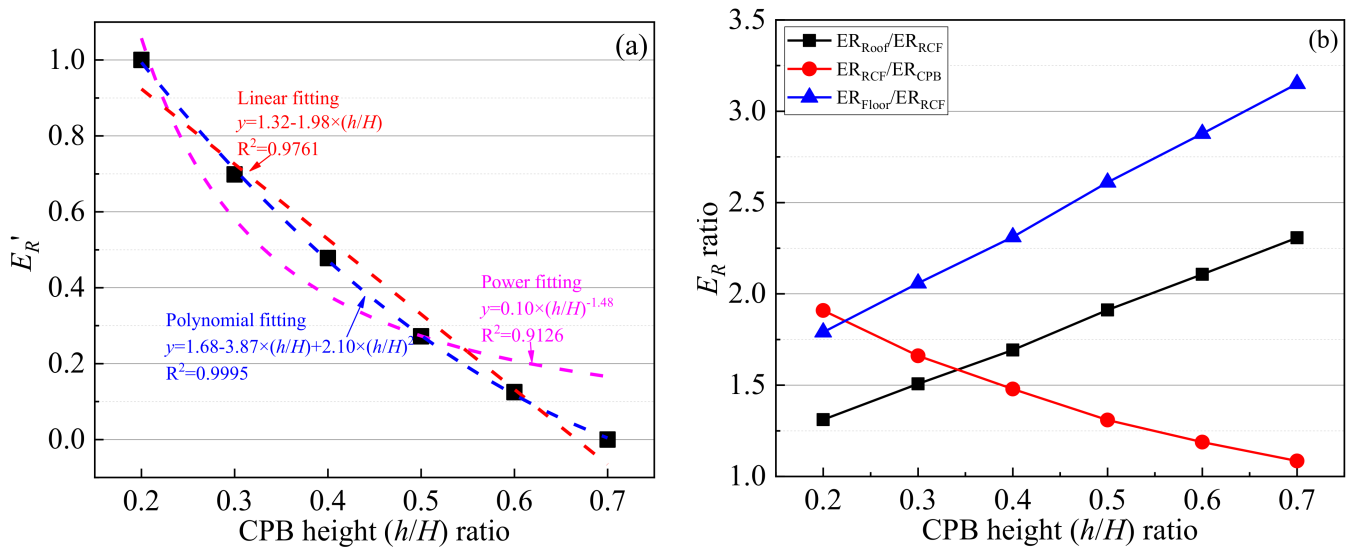where $E_R{}'$ is the normalized value of elastic modulus of the RCF material.

Figure 5. Elastic modulus of RCF material: (**a**) E_R and h/H ratio; (**b**) E_R ratio and h/H ratio.

Similarly, the E_R ratio of the RR and FR to the RCF material represents the E_R deterioration degree of the RCF material on the RR and FR, respectively. The E_R ratio of the RCF material to the CPB represents the E_R strengthening degree of the RCF material on the CPB. Figure 5b shows the E_R ratio. The ER_{Roof}–ER_{RCF} ratio and the ER_{Floor}–ER_{RCF} ratio increased with the increase in the CPB height ratio and the ER_{RCF}–ER_{CPB} ratio decreased with the increase in the CPB height ratio. When the CPB height ratio increased from 0.2 to 0.7, the ER_{Roof}–ER_{RCF} ratio and the ER_{Floor}–ER_{RCF} ratio increased from 1.311 to 2.307 and 1.790 to 3.151, and the ER_{RCF}–ER_{CPB} ratio decreased from 1.909 to 1.085.

3.1.3. Peak Strain

Figure 6 shows the relationship between the peak strain of the RCF material (the strain at its peak stress point) and the CPB height ratio. The peak strain of the RCF material first decreased and then increased with the increase in the CPB height ratio. When the CPB height ratio increased from 0.2 to 0.5, the peak strain of the RCF material decreased from 0.695% to 0.510%. When the CPB height ratio increased from 0.5 to 0.7, the peak strain of the RCF material began to increase from 0.510% to 0.577%. The peak strain of the RCF material reached its maximum value of 0.695% when the CPB height ratio was 0.2 and its minimum value of 0.510% when the CPB height ratio was 0.5. When the CPB height ratio was in the range of 0.2–0.5, with the increase in the CPB height ratio, the proportion of the rock layer (i.e., the roof rock and floor rock layers) decreased, the proportion of the CPB layer increased, and the decrease in the strength of the RCF material was greater than that of the elastic modulus. Therefore, the peak strain of the RCF material decreased gradually at this stage. When the CPB height ratio was greater than 0.5, the CPB layer became the main part of the RCF material and the influence of the rock layer on the RCF material was much less than that of the CPB layer. At this time, the decrease in the elastic modulus was the main change in the RCF material and the change in its strength was very small (Section 3.1.1). Therefore, with the increase in the proportion of the CPB layer, the peak strain of the RCF material began to increase.
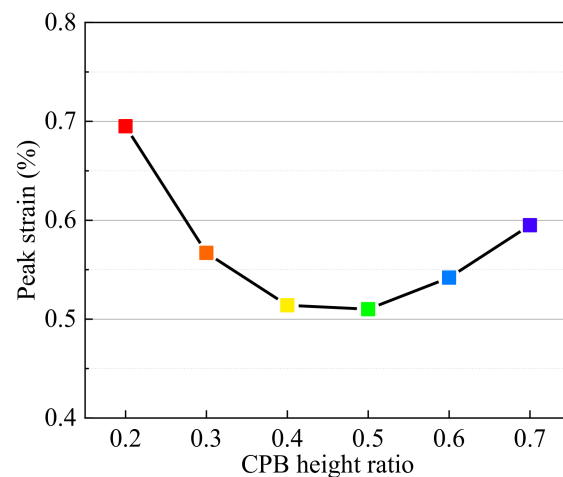
Figure 6. Peak strain and CPB height ratio of RCF material.

3.2. AE Ring Count Characteristic of RCF Materials

The stress-AE ring count characteristics of RCF materials with different CPB height ratios are shown in Figure 7. As can be seen from Figure 7, the change law of the AE ring counts of the different RCF samples is basically similar. At the initial stage of loading, the stress was small, the primary cracks in the RCF sample were closed, no new cracks were generated, and the AE ring count was small. With the increase in the load, the internal stress of the RCF sample increased, the primary crack began to expand, new cracks began to sprout, and the AE ring count increased slowly. With the continued increase in the load, the internal stress of the RCF sample gradually exceeded its yield limit, the sample showed yield failure, the cracks began to expand rapidly, the AE ring count increased rapidly, and the AE accumulation curve rose rapidly. When the load exceeded the ultimate load of the RCF sample, macro cracks began to appear, the number of the AE ring count continued to increase, and the AE ring count accumulation curve increased almost linearly. With the further application of the load, the RCF sample became unstable and damaged, but there was still a small AE ring count due to the cohesion and friction in the sample.

Furthermore, Figure 7a,b show that there were multiple peaks in the AE ring count curves of the RCF material, indicating that there were stress concentration phenomena in the RCF sample, resulting in a sudden increase in the cracks in the sample, and the stress and AE ring count accumulation curves show a steep upward trend. It can be seen from Figure 7c–f that the AE ring count curve of the RCF material continued to rise without multiple peaks and the stress and AE ring count accumulation curves showed a smooth upward trend.

Figure 8 shows the relationship between the AE cumulative ring count of the RCF material at its peak stress point and the CPB height ratio. The AE cumulative ring count decreased with the increase in the CPB height ratio. When the CPB height ratio increased from 0.2 to 0.7, the AE cumulative ring count of the RCF material at the peak stress point decreased from 925 to 735. When the CPB height ratio increased, the overall strength of the RCF material decreased, the internal released energy decreased, and the AE cumulative ring count decreased.
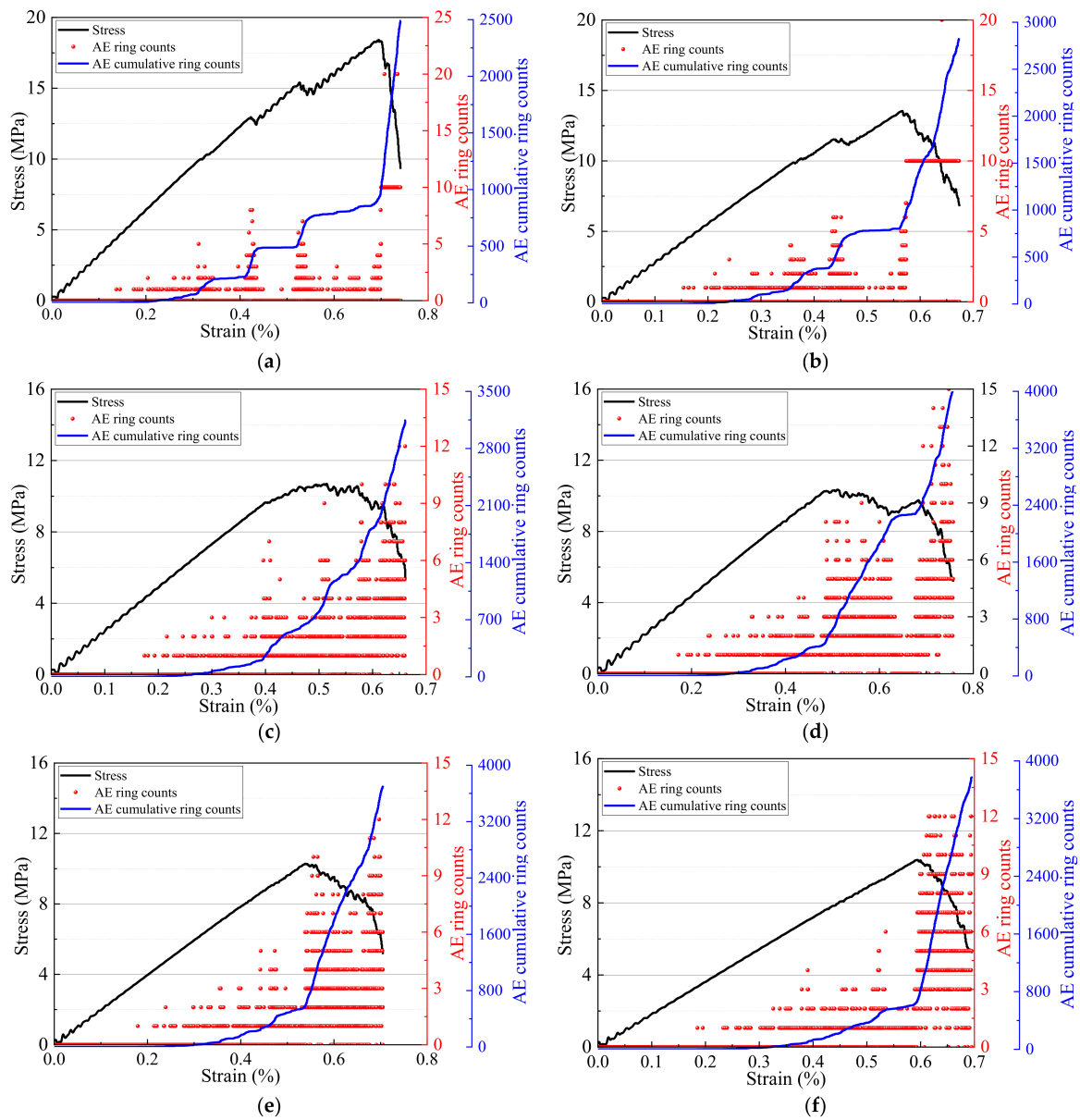
Figure 7. Stress-AE ring count–AE cumulative ring count curves: (**a**–**f**): RCF2–RCF7.
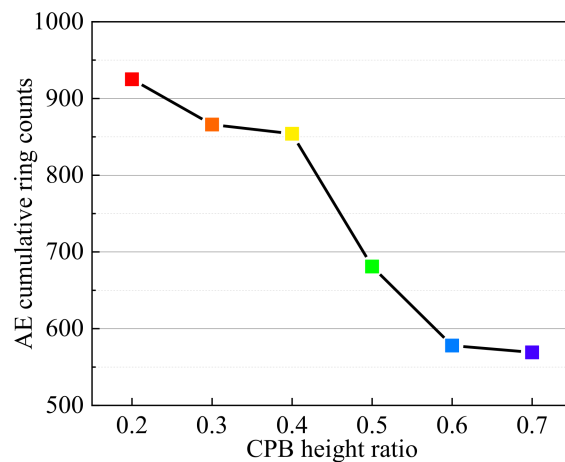

Figure 8. AE cumulative ring count of RCF material at peak point.

3.3. Energy Dissipation Mechanism of RCF Materials

The deformation and failure of the RCF samples is a process of continuous energy exchange with the external environment. During the loading process, the RCF sample continuously absorbs energy and converts that energy into releasable elastic energy and dissipated energy. When the energy that is absorbed by the RCF sample exceeds its energy storage limit, part of the releasable elastic energy will be released, resulting in the overall failure of the RCF sample. According to energy conservation [35,50]:

$$U_T = U_E + U_D \tag{3}$$

where U_T is the total energy that is absorbed by the sample, U_E is the releasable elastic properties that are stored in the sample, and U_D is the dissipated energy of the sample.

Figure 9 shows the internal energy evolution process of the RCF sample. In the initial stage, the RCF sample absorbs the energy and converts it into releasable elastic energy, which is stored in the sample. In the middle stage, the releasable elastic energy that is stored in the RCF sample exceeds its elastic limit and part of that absorbed energy is converted into dissipated energy and released to the outside world. In the later stage, the energy that is stored inside the RCF sample exceeds its energy storage limit, resulting in the failure of the sample and the energy that is stored in the sample is quickly released to the outside. The energy balance equation of the RCF sample under uniaxial compression is [50–52]:

$$U_T = \int_0^\varepsilon \sigma d\varepsilon \tag{4}$$

$$U_E = \frac{\sigma^2}{2E_R} \tag{5}$$

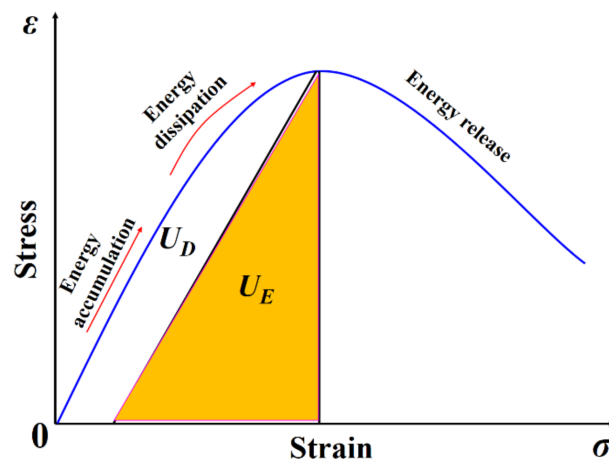where E_R is the elastic modulus of the RCF sample.

Figure 9. RCF sample energy evolution process.

According to Equations (4) and (5), the evolution curves of the U_T, U_E, and U_D can be calculated combined with the stress-strain curve of the RCF sample and the results of these calculations are shown in Figure 10. In the initial stage, all of the energy that was absorbed by the sample was converted into releasable elastic energy, all of the deformation of the sample was elastic deformation, and there was no damage inside the sample, so the dissipated energy at this stage was almost zero. In the middle stage, the load gradually exceeded the yield limit of the sample, the damage began to occur in the sample, and the dissipated energy began to increase. In the later stage, the damage to the sample accumulated rapidly, the releasable elastic energy began to decrease and the dissipated energy increased rapidly.
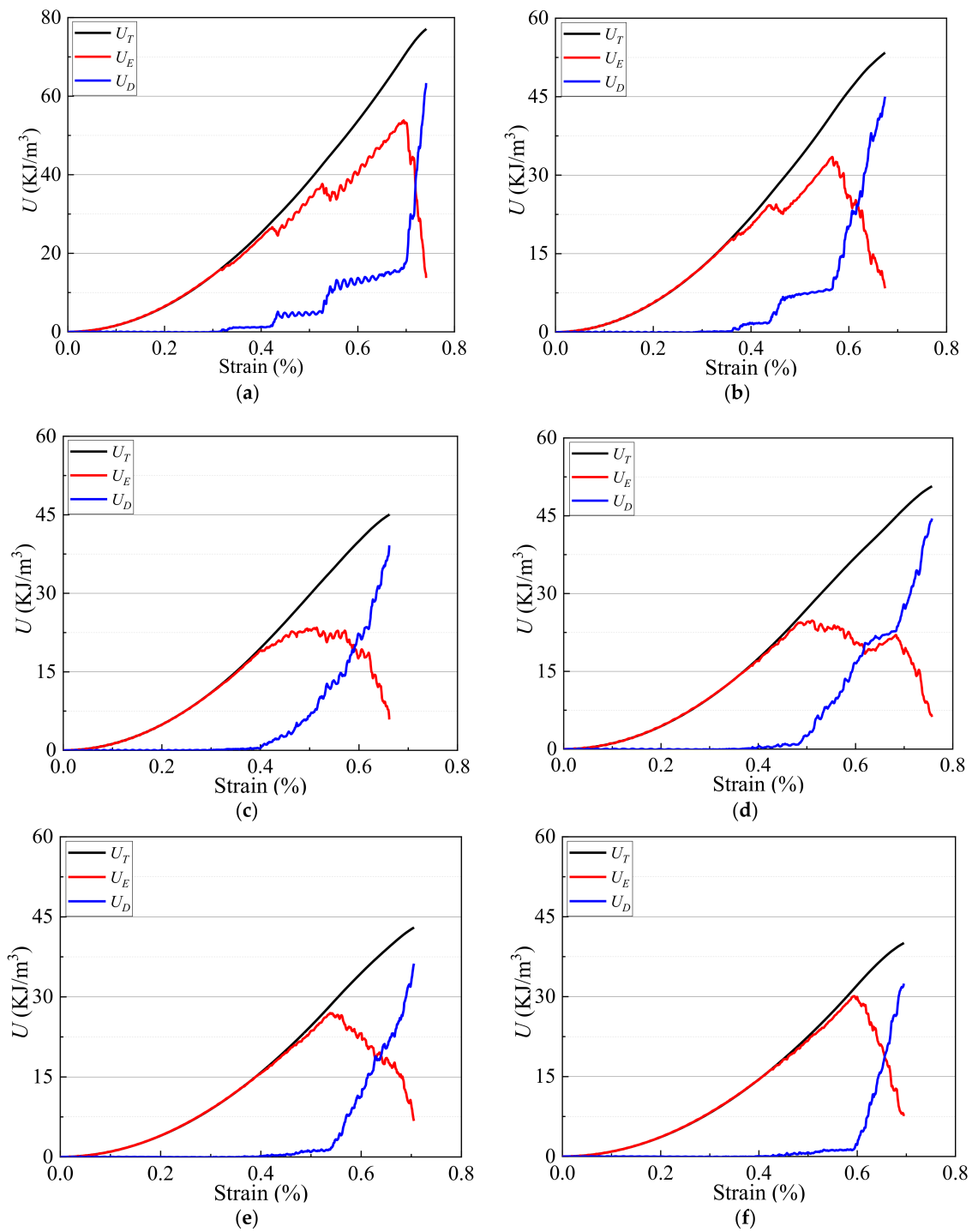
Figure 10. Energy evolution of different RCF samples: (**a**–**f**): RCF2–RCF7.

Figure 11 shows the three energies evolution curves with strain. Figure 11a shows that the evolution of the total energy U_T that was absorbed by the different RCF samples was basically similar, increasing slowly at first and then rapidly. In addition, the greater the CPB height ratio, the slower the cumulative speed of the U_T, and the smaller the U_T. Figure 11b shows that the storage process of the U_E of the different RCF samples was also basically similar. In the initial stage, the sample was compacted and the U_E accumulated slowly. In the middle stage, elastic deformation occurred, the U_E accumulated rapidly, and the elastic energy curve rose almost linearly. In the later stage, the load exceeded the bearing limit of the sample, resulting in the failure of the sample, the sample's release of energy to the

outside, and a rapid decrease in the elastic energy. Figure 11c shows that, in the initial stage, there was no damage inside the sample and the U_D was almost zero. In the middle stage, the damage to the sample gradually accumulated and the U_D began to increase slowly. In the later stage, the damage accumulated rapidly and the U_D increased rapidly. The dissipated energy curves of the different RCF samples are not very distinguishable.
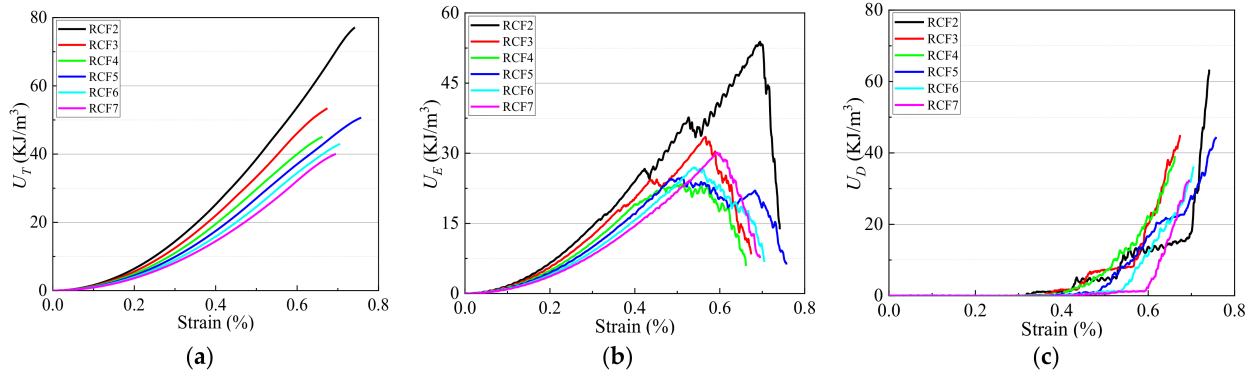

Figure 11. Different types energy evolution of RCF samples: (**a**) U_T; (**b**) U_E; (**c**) U_D.

Figure 12 shows the variation of the three energies at the peak point of the RCF samples with their CPB height ratio. Figure 12a shows that the U_T, U_E, and U_D at the peak point decreased with the increase in the CPB height ratio. When the CPB height ratio was 0.2, the U_T, U_E, and U_D were 70.07 KJ/m^3, 53.84 KJ/m^3, and 16.23 KJ/m^3, respectively. When the CPB height ratio increased to 0.3, the three energies decreased to 41.80 KJ/m^3, 33.47 KJ/m^3, and 8.33 KJ/m^3, respectively. When the CPB height ratio increased to 0.7, the three energies decreased to 31.57 KJ/m^3, 30.09 KJ/m^3, and 1.48 KJ/m^3, respectively. With the increase in the CPB height ratio, the proportion of CPB in the RCF samples increased. However, the energy storage capacity of the CPB was smaller than that of the rock. Therefore, the three energies gradually decreased with the increase in the CPB height ratio. Figure 12b shows the relationship between the energy ratio and the PCB height ratio. Overall, with the increase in the CPB height ratio, the ratio of the elastic energy to the total energy (U_E–U_T) increased, the ratio of the dissipated energy to the total energy (U_D–U_T) decreased, and the ratio of the elastic energy to the dissipated energy (U_E–U_D) increased. When the CPB height ratio was 0.2, the U_E–U_T, the U_D–U_T, and the U_E–U_D were 0.77, 0.23, and 3.32, respectively. When the CPB height ratio increased to 0.7, the U_E–U_T and the U_E–U_D increased to 0.90 and 9.43, respectively, and the U_D–U_T decreased to 0.10.
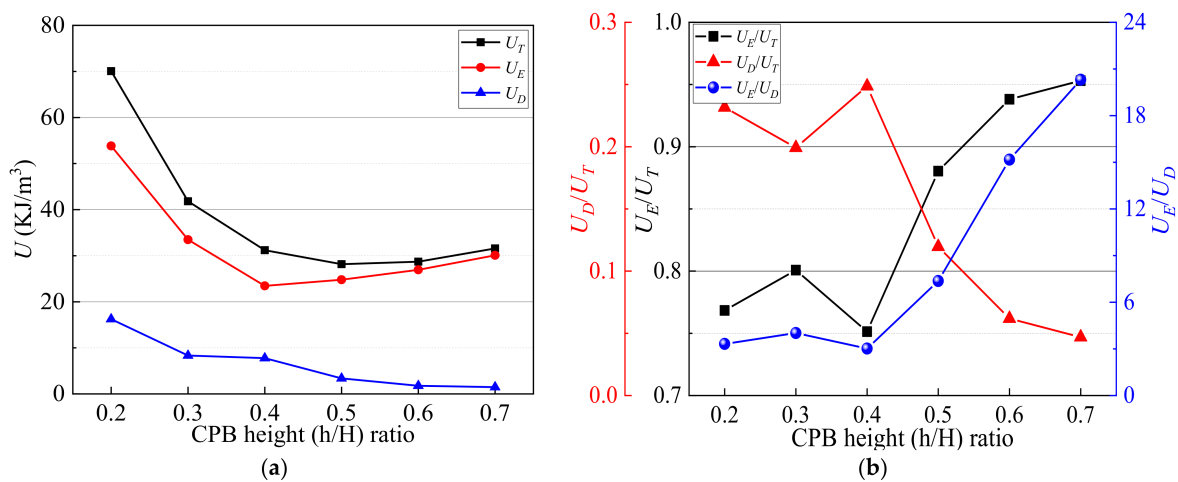

Figure 12. Energy dissipation and energy dissipation ratio of RCF sample at peak point: (**a**) energy dissipation; (**b**) energy dissipation ratio.

3.4. Damage Constitutive Model of RCF Materials

3.4.1. Model Construction

In order to study the damage evolution mechanism of RCF composite materials during uniaxial compression, the damage model that is based on AE ring count [53,54] shows that: assuming that the section area A is destroyed, the cumulative AE ring count of the RCF composite material is N. Then, when the damaged area of the section reaches A_d, the AE cumulative ring count is:

$$N_f = \frac{A_d}{A} N \qquad (6)$$

It can be considered that the damage variable D_A in RCF combination materials is:

$$D_A = (1 - \frac{\sigma_r}{\sigma_p}) \frac{N_f}{N} \qquad (7)$$

where D_A is the damage variable of the RCF material based on the AE ring count, σ_r is the residual stress of the RCF material, σ_p is the peak stress of the RCF material, N_f is the AE cumulative ring count, and N is the total AE ring count.

Then, the damage constitutive model of RCF composite materials, based on the AE ring count, can be expressed as:

$$\sigma = E\varepsilon(1 - D_A) = E\varepsilon[1 - (1 - \frac{\sigma_r}{\sigma_p}) \frac{N_f}{N}] \qquad (8)$$

In addition, according to the research of Ma et al. [50,54], the damage variable of RCF composite materials can be characterized by the energy dissipation relationship:

$$D_E = (1 - \frac{\sigma_r}{\sigma_p}) \times \frac{U_D}{U_{D\text{max}}} \times (1 + \frac{U_{Dp}}{U_{Tp}}) \qquad (9)$$

where D_E is the damage variable of the RCF material based on the energy dissipation, U_D is the dissipation energy, $U_{D\text{max}}$ is the cumulative dissipated energy, U_{Dp} is dissipation energy at the peak point, and U_{Tp} is total energy that is input into the RCF material at the peak point.

The damage constitutive model of RCF material, based on the energy dissipation under uniaxial compressive:

$$\sigma = (1 - D_E)E\varepsilon = \left[1 - (1 - \frac{\sigma_r}{\sigma_p}) \times \frac{U_D}{U_{D\text{max}}} \times (1 + \frac{U_{Dp}}{U_{Tp}})\right] E\varepsilon \qquad (10)$$

3.4.2. Model Verification

Based on the findings of other scholars [50,53–55], this paper constructs two damage constitutive models of RCF material under uniaxial compression, based on acoustic emission and energy dissipation; however, the rationality and reliability of these models still need to be fully verified. Figure 13 shows the comparison results between the two model curves that were constructed in this paper and the test curve.

The damage constitutive models that are based on acoustic emission and energy dissipation highly coincide with the test curve, indicating that the two damage constitutive models that were constructed in this paper are applicable and can provide reliable theoretical support for subsequent damage evolution analysis.
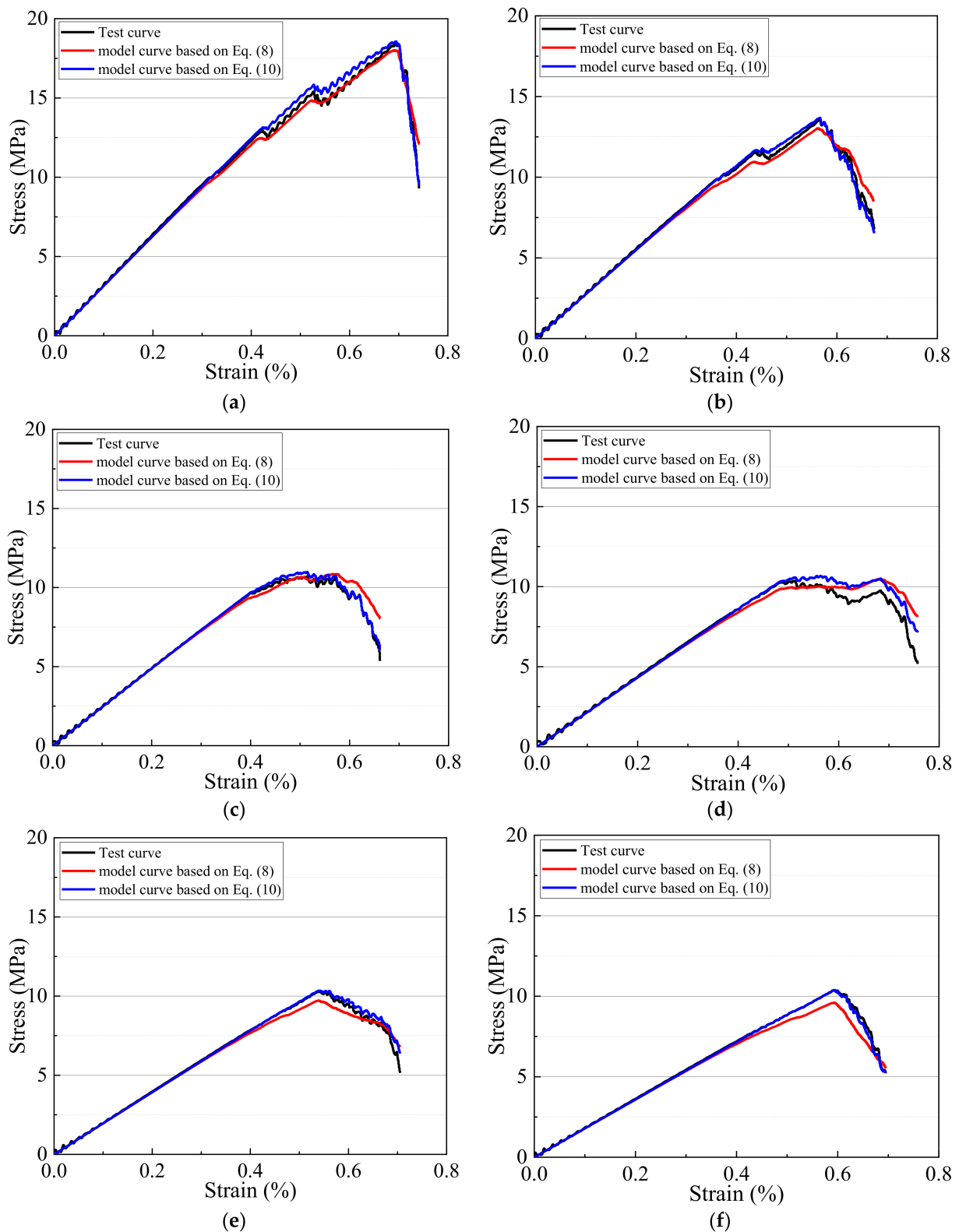
Figure 13. Damage constitutive model curves and tests curves: (**a**–**f**): RCF2-RCF7.

3.4.3. Damage Evolution

According to the established damage evolution Equations (8) and (10), the damage evolution curve of RCF materials can be calculated, and the results of these calculations are shown in Figure 14. The damage evolution law that is based on acoustic emission

and energy dissipation is basically the same. In the whole loading process, the damage evolution process of RCF materials can be divided into three stages:

(1) Stage 1: At this stage, the original pore structure in the RCF sample had been compacted and the layered structural plane had been closed. The original pores in the sample began to expand, while new microcracks gradually formed, the sample's damage began to accumulate slowly, and the damage curve began to grow slowly. The damage evolution curve of RCF material has an obvious correlation with the CPB height ratio. It can be seen from the figure that the smaller the CPB height ratio, the faster the damage evolution rate. In the initial compression stage, the sample with a larger CPB height ratio could bear greater deformation, but it was not easy to damage. On the contrary, a smaller CPB height ratio allowed the deformation to reach the upper limit quickly and damage occurred in this case first.

(2) Stage 2: This stage is the stage of damage-stable evolution. Under the load, the internal primary pores and new cracks developed steadily, and the damage accumulated stably. At this time, it could be inferred that the damage accumulation of the central CPB was close to its upper limit, the rocks at both ends were compressed, and a small number of fractures expanded in the rocks at both ends. The CPB height ratio had little effect on the damage evolution process and the damage evolution curves of the different RCF samples had no obvious difference.

(3) Stage 3: This stage is the stage of rapid damage accumulation. As the load that was on the RCF material gradually exceeded its peak load, the overall stable structure of the RCF sample had been destroyed, the internal crack and pore structure expanded rapidly and formed macro cracks, and the internal damage to the sample accumulated rapidly. At this stage, there was no significant difference in the damage evolution curves of the different RCF samples.
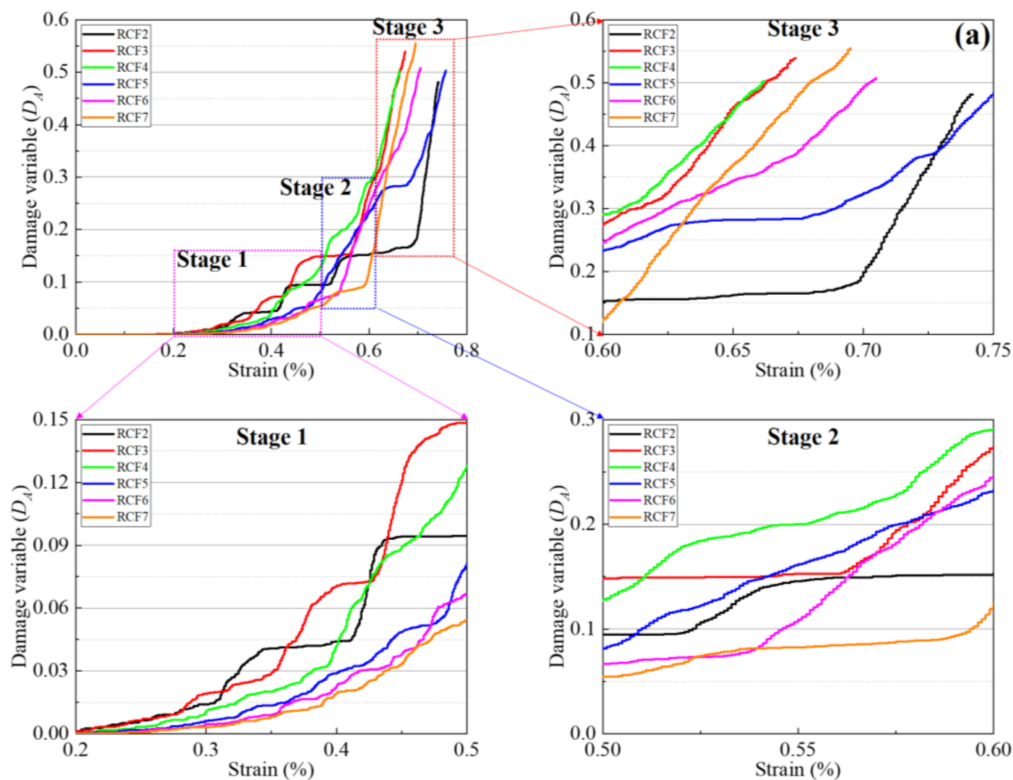

Figure 14. *Cont.*
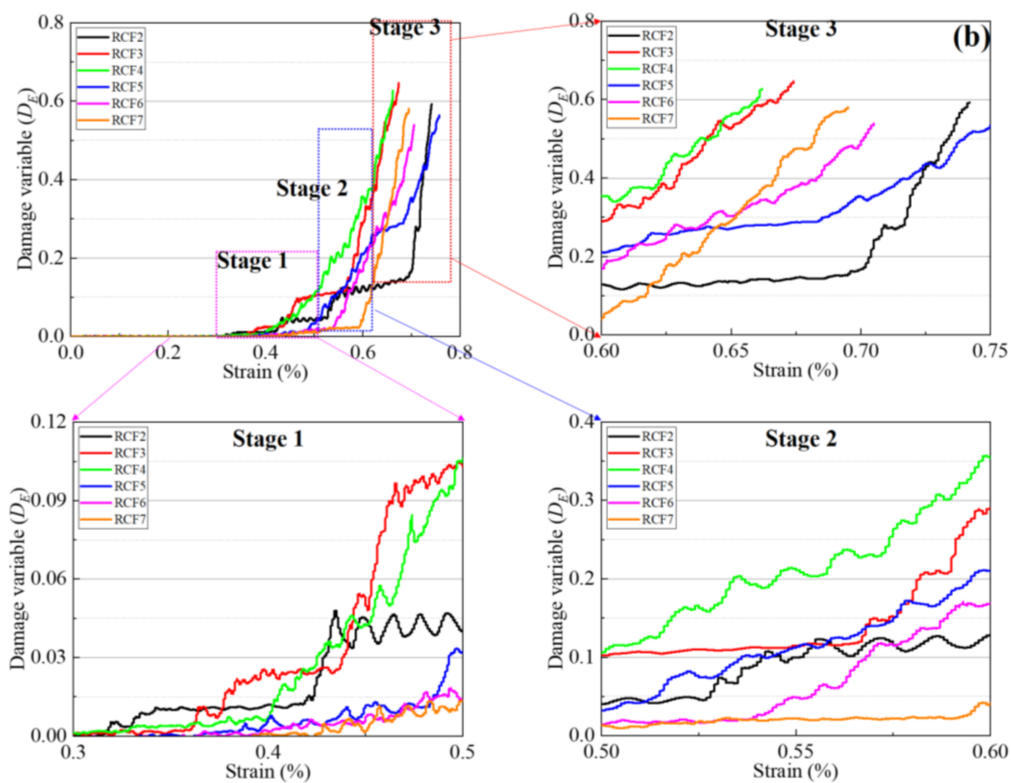
Figure 14. Damage evolution characteristics: (**a**) Damage variable D_A; (**b**) Damage variable D_E.

4. Discussion

According to the analyses in Section 3.1, the CPB height ratio in the RCF layered composite material has an important impact on its mechanical properties. When the proportion of the CPB height increases, the (*UCS* and elastic modulus of the RCF material continues to decrease, while the peak strain of the RCF material first decreases and then increases. These results are shown in Figure 15.
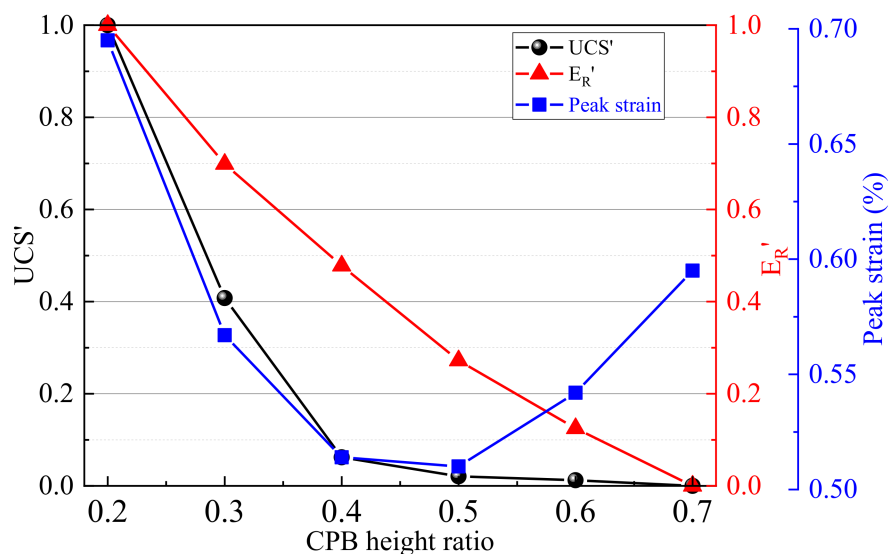

Figure 15. Composite diagram of CPB height ratio, (*UCS'*, E_R', and peak strain.

In analyzing the deep-seated reasons for these results, it was found that the increase in the CPB height is equivalent to increasing the proportion of the weak medium material in RCF composite material. Under a load, the greater the proportion of weak medium material,

the greater the probability of damage. Furthermore, the more damage that is present in a weak medium and the easier the damage in that weak medium evolves into a strong medium, the greater the likelihood of the overall failure of the RCF layered composite material. Therefore, the strength of the RCF material in question is lesser.

In addition, as discovered through the analyses in Section 3.1.2, the stiffness of the CPB material was found to be much less than that of the rock material. When the two media are non-uniformly combined, the stiffness of the weak medium material determines the lower limit of the stiffness of the RCF layered composite material, while the stiffness of the strong medium material determines the upper limit of the stiffness of the RCF material. Obviously, when the proportion of the weak medium is larger, the lower limit of the stiffness of the RCF material is smaller. On the contrary, when the proportion of the weak medium is smaller, that is, the proportion of strong medium is larger, the upper limit of the stiffness of the RCF composite material is larger.

However, there are some differences between the peak strain of an RCF material and its (*UCS* and elastic modulus. As we all know, the deformation of CPB material is greater than that of rock material. When the proportion of the CPB material increases, the overall deformation capacity of the RCF material increases and its peak strain also increases. When the proportion of the CPB material exceeds a certain degree, although the overall deformation capacity of the RCF material is improved its overall strength is also significantly reduced. Under the action of a load, the deformation of the central CPB material is far from reaching its peak deformation and the RCF material reaches its peak strength, resulting in a decreasing trend in the peak strain of the RCF material.

Combined with the analyses in Sections 3.1.1 and 3.1.2. The (*UCS'* and E_R' of RCF layered composite materials have a common variation law, both of which decrease with the increase in the proportion of a weak medium, and there is a certain internal relationship between the strength and stiffness characteristics of the material itself. In order to deeply analyze the internal correlation mechanism between (*UCS'* and E_R', the two are discussed together. The results are shown in Figure 16.
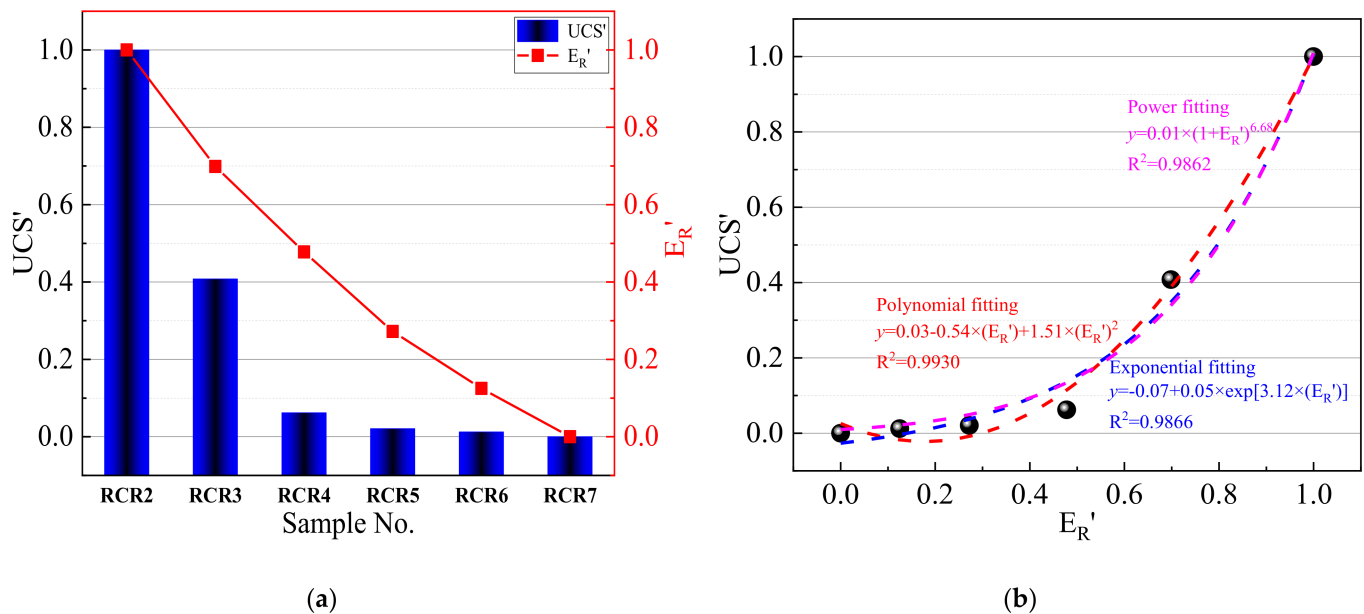

Figure 16. Relationship between (*UCS'* and E_R' of RCF materials.

It can be seen from Figure 16a that the (*UCS'* and E_R' of the RCF materials have the same change law and both decrease with the increase in the CPB height ratio (RCF2–RCF7). It can be seen from Figure 16b that the (*UCS'* of the RCF material increased with the increase in E_R'. When the E_R' of the RCF materials was 0, the (*UCS'* of the RCF material was 0;

when the E_R' increased to 0.13, 0.27, 0.48, 0.70, and 1.0, the (UCS' increased to 0.01, 0.02, 0.06, 0.41, and 1.0, respectively. Three functions were used to fit the relationship between (UCS' and E_R' of the RCF material. The results show that the polynomial function can better characterize the functional relationship between them:

$$(UCS' = 0.03 - 0.54 \times (E_R') + 1.51 \times (E_R')^2 \tag{11}$$

Under the action of a load, the material continuously absorbs energy from the outside and stores it. When the absorbed energy exceeds the energy storage limit of the material, the material will be damaged and release energy to the outside; the process of releasing energy usually produces acoustic emission signals. Therefore, there is a close relationship between the energy dissipation, damage evolution, and acoustic emission of materials. Figure 17 shows the stress–damage–AE–energy dissipation composite diagram of the RCF4 and RCF5 samples.
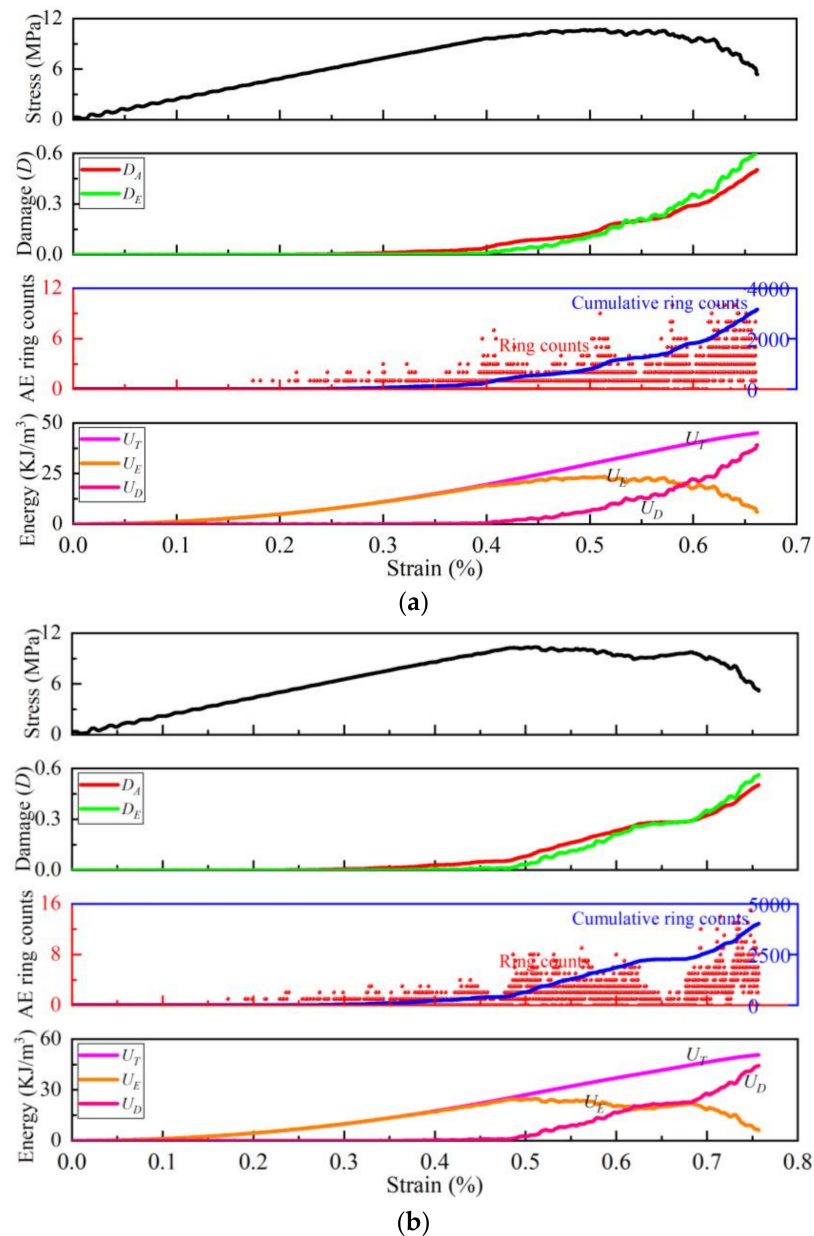

Figure 17. The stress–damage–AE–energy dissipation composite diagram: (**a**) RCF4 sample; (**b**) RCF5 sample.

Taking the RCF4 sample (Figure 17a) as an example, in the initial loading stage (in which the strain increases from 0 to 0.2%), the internal primary pores of the sample were compacted and the layered structural plane was closed. Although the sample continuously absorbed the energy (the U_E increased from 0 to 4.98 KJ/m^3), the sample did not produce damage at this stage ($D = 0$); however, sporadic AE signals were generated during the compaction of the internal primary pores. When the load was continuously applied, the RCF4 sample entered the linear elastic stage (as the strain increased from 0.2% to 0.4%), the elastic energy continued to accumulate (the U_E increased from 4.98 to 19.6 KJ/m^3), but the dissipated energy did not increase, the sample was not damaged, and a small amount of AE signals were still being monitored (the cumulative ring count was 314). Subsequently, the energy that was accumulated in the RCF4 sample gradually reached its energy storage limit. The RCF4 sample went through the yield stage (in which the strain increased from 0.4% to 0.5%). At this time, the RCF4 sample began to dissipate energy (the U_D increased from 0 to 6.7 KJ/m^3) and the internal damage began to accumulate slowly (the damage value D increased from 0 to 0.13). At the same time, a large number of AE signals were monitored (the cumulative ring count reached 860). Finally, the RCF4 sample entered the post-peak stage, the elastic energy inside the sample began to decrease gradually, the dissipated energy increased rapidly, and the sample entered the stage of rapid damage accumulation. At the same time, the sample began to release a large number of AE signals to the outside world.

5. Conclusions

In this paper, the mechanical properties, AE ring count characteristics, and energy dissipation mechanism of RCF layered composite materials were studied by uniaxial compression AE tests. Based on the AE ring counts and energy dissipation, two damage constitutive models of RCF materials have been established and the damage evolution of RCF materials was deeply analyzed. The main conclusions are as follows:

(1) The (UCS and E_R of the RCF samples were lower than those of the RR and FR, but higher than those of the CPB. With the increase in the CPB height ratio, the (UCS and E_R of the RCF samples showed a decreasing trend. The CPB height ratio had an exponential function relationship with the (UCS and a polynomial function relationship with E_R. The (UCS increased as a polynomial function with the increase in the E_R.

(2) The change law of the AE ring counts of the different RCF samples was basically similar. The AE ring count first grew slowly, then increased rapidly, and finally maintained a high-speed increase. The AE cumulative ring count at the peak point of the RCF sample decrease with the increase in the CPB height ratio.

(3) At first, the elastic energy U_E of the RCF sample began to accumulate slowly, then the dissipated energy U_D began to increase. Finally, the U_E began to decrease and the U_D increased almost linearly. The U_T, U_E, and U_D at the peak point showed a decreasing trend with the increase in the CPB height ratio. With the increase in the CPB height ratio, the U_E–U_T ratio and the U_D–U_T ratio decreased and the U_E–U_D ratio increased.

(4) Two damage constitutive models were established based on the AE ring counts and energy principle. The verification results show that the model that was constructed in this paper is reasonable and reliable. The damage evolution process of RCF materials can be divided into three stages: the slow damage accumulation stage, stable damage growth stage, and rapid damage accumulation stage.

(5) The AE ring counts and energy dissipation are closely related to internal damage evolution. First, the AE ring count accumulated slowly, the U_E increased slowly, and there was almost no damage evolution. Subsequently, the AE ring count accumulated rapidly, U_D increased slowly, and damage slowly evolved. Finally, the AE ring count maintained high-speed accumulation, U_E began to decrease, U_D increased rapidly, and damage rapidly evolved.

References

1. Xue, G.L.; Yilmaz, E.; Song, W.D.; Cao, S. Mechanical, flexural and microstructural properties of cement-tailings matrix composites: Effects of fiber type and dosage. *Compos. Part B Eng.* **2019**, *172*, 131–142. [CrossRef]
2. Wang, J.; Fu, J.X.; Song, W.D.; Zhang, Y.F. Viscosity and Strength Properties of Cemented Tailings Backfill with Fly Ash and Its Strength Predicted. *Minerals* **2021**, *11*, 78. [CrossRef]
3. Li, J.J.; Yilmaz, E.; Cao, S. Influence of industrial solid waste as filling material on mechanical and microstructural characteristics of cementitious backfills. *Constr. Build. Mater.* **2021**, *299*, 124288. [CrossRef]
4. Xue, G.L.; Yilmaz, E.; Song, W.D.; Cao, S. Analysis of internal structure behavior of fiber reinforced cement-tailings matrix composites through X-ray computed tomography. *Compos. Part B Eng.* **2019**, *175*, 107091. [CrossRef]
5. Zhao, K.; Huang, M.; Yan, Y.J.; Wan, W.L.; Ning, F.J.; Zhou, Y.; He, Z.W. Mechanical properties and synergistic deformation characteristics of tailings cemented filling assembled material body with different cement-tailings ratios. *Chin. J. Rock Mech. Eng.* **2021**, *40* (Suppl. 1), 2781–2789.
6. Cao, S.; Xue, G.L.; Yilmaz, E.; Yin, Z.Y.; Yang, F.D. Utilizing concrete pillars as an environmental mining practice in underground mines. *J. Clean. Prod.* **2021**, *278*, 123433. [CrossRef]
7. Tosun-Felekoglu, K.; Felekoglu, B. Effects of fiber–matrix interaction on multiple cracking performance of polymeric fiber reinforced cementitious composites. *Compos. Part B Eng.* **2013**, *52*, 62–71. [CrossRef]
8. Fang, K.; Fall, M. Shear Behaviour of Rock-Tailings Backfill Interface: Effect of Cementation, Rock Type, and Rock Surface Roughness. *Geotech. Geol. Eng.* **2021**, *39*, 1753–1770. [CrossRef]
9. Xiu, Z.G.; Wang, S.H.; Wang, F.L.; Ren, F.Y.; Vantuan, N. Comparative experimental study on the shear behavior of cemented paste backfill and surrounding rock-backfill interface. *Chin. J. Rock Mech. Eng.* **2021**, *40*, 1628–1642.
10. Cheng, A.P.; Shu, P.F.; Zhang, Y.S.; Wang, P.; Wang, M.X. Acoustic emission characteristics and damage constitution of backfill-surrounding rock combination. *J. Min. Saf. Eng.* **2020**, *37*, 1238–1245.
11. Sarfarazi, V.; Abharian, S.; Ghorbani, A. Physical test and PFC modelling of rock pillar failure containing two neighboring joints and one hole. *Smart Struct. Syst.* **2021**, *27*, 123–137.
12. Sarfarazi, V.; Abharian, S.; Ghalam, E.Z. Physical test and PFC2D simulation of the failure mechanism of echelon joint under uniaxial compression. *Comput. Concr.* **2021**, *27*, 99–109.
13. Wang, Y.R.; Lu, H.J.; Wu, J. Experimental investigation on strength and failure characteristics of cemented paste backfill-rock composite under uniaxial compression. *Constr. Build. Mater.* **2021**, *304*, 124629. [CrossRef]
14. He, Z.W.; Zhao, K.; Yan, Y.J.; Ning, F.J.; Zhou, Y.; Song, Y.F. Mechanical response and acoustic emission characteristics of cement paste backfill and rock combination. *Constr. Build. Mater.* **2021**, *288*, 123119. [CrossRef]
15. Wu, W.L.; Xu, W.B.; Zuo, J.P. Effect of inclined interface angle on shear strength and deformation response of cemented paste backfill-rock under triaxial compression. *Constr. Build. Mater.* **2021**, *279*, 122478.
16. Fang, K.; Cui, L.; Fall, M. A coupled chemo-elastic cohesive zone model for backfill-rock interface. *Comput. Geotech.* **2020**, *125*, 103666. [CrossRef]
17. Fang, K.; Fall, M.; Cui, L. Thermo-chemo-mechanical cohesive zone model for cemented paste backfill-rock interface. *Eng. Fract. Mech.* **2021**, *244*, 107546. [CrossRef]
18. Yu, X.; Kemeny, J.; Tan, Y.Y.; Song, W.D.; Huang, K. Mechanical properties and fracturing of rock-backfill composite specimens under triaxial compression. *Constr. Build. Mater.* **2021**, *304*, 124577. [CrossRef]
19. Zhao, L.D. Numerical investigation on the mechanical behaviour of combined backfill-rock structure with KCC model. *Constr. Build. Mater.* **2021**, *283*, 122782. [CrossRef]
20. Zhao, K.; He, Z.W.; Ning, F.J.; Zhou, Y.; Yan, Y.J.; Wang, Y.L.; Wang, J.Q. Acoustic Emission Characteristics of Cementitious Material with Different Cement-Tailing Ratio. *J. Chin. Ceram. Soc.* **2021**, *49*, 2462–2469.
21. Liu, W.; Ma, L.Q.; Sun, H.; Khan, N.M. An experimental study on infrared radiation and acoustic emission characteristics during crack evolution process of loading rock. *Infrared Phys. Technol.* **2021**, *118*, 103864. [CrossRef]

22. Liu, X.L.; Liu, Z.; Li, X.B.; Gong, F.Q.; Du, K. Experimental study on the effect of strain rate on rock acoustic emission characteristics. *Int. J. Rock Mech. Min. Sci.* **2020**, *133*, 104420. [CrossRef]

23. Liu, J.P.; Wang, R.; Lei, G.; Si, Y.T.; Xu, S.D.; Li, Y.H. Studies of stress and displacement distribution and the evolution law during rock failure process based on acoustic emission and microseismic monitoring. *Int. J. Rock Mech. Min. Sci.* **2020**, *132*, 104384. [CrossRef]

24. Lin, Q.B.; Cao, P.; Cao, R.H.; Lin, H.; Meng, J.J. Mechanical behavior around double circular openings in a jointed rock mass under uniaxial compression. *Arch. Civ. Mech. Eng.* **2020**, *20*, 19. [CrossRef]

25. Wang, J.; Fu, J.X.; Song, W.D.; Zhang, Y.F.; Wu, S. Acoustic emission characteristics and damage evolution process of layered cemented tailings backfill under uniaxial compression. *Constr. Build. Mater.* **2021**, *295*, 123663. [CrossRef]

26. Cheng, A.P.; Shu, P.F.; Deng, D.Q.; Zhou, C.S.; Huang, S.B.; Ye, Z.Y. Microscopic acoustic emission simulation and fracture mechanism of cemented tailings backfill based on moment tensor theory. *Constr. Build. Mater.* **2021**, *308*, 125069. [CrossRef]

27. Zhou, Y.; Yan, Y.J.; Zhao, K.; Yu, X.; Song, Y.F.; Wang, J.Q.; Suo, T.Y. Study of the effect of loading modes on the acoustic emission fractal and damage characteristics of cemented paste backfill. *Constr. Build. Mater.* **2021**, *277*, 122311. [CrossRef]

28. Zhao, K.; Yu, X.; Zhu, S.T.; Yan, Y.J.; Zhou, Y.; He, Z.W.; Song, Y.F.; Huang, M. Acoustic emission fractal characteristics and mechanical damage mechanism of cemented paste backfill prepared with tantalum niobium mine tailings. *Constr. Build. Mater.* **2020**, *258*, 119720. [CrossRef]

29. Wang, Y.Y.; Deng, H.C.; Deng, Y.; Chen, K.P.; He, J.H. Study on crack dynamic evolution and damage-fracture mechanism of rock with pre-existing cracks based on acoustic emission location. *J. Pet. Sci. Eng.* **2021**, *201*, 108420. [CrossRef]

30. Behera, S.K.; Mishra, D.P.; Singh, P.; Mishra, K.; Mandal, S.K.; Ghosh, C.N.; Kumar, R.; Mandal, P.K. Utilization of mill tailings, fly ash and slag as mine paste backfill material: Review and future perspective. *Constr. Build. Mater.* **2021**, *309*, 125120. [CrossRef]

31. Souyang, H.; Huang, Y.; Zhou, N.; Li, J.; Gao, H.; Guo, Y. Experiment on hydration exothermic characteristics and hydration mechanism of sand-based cemented paste backfill materials. *Constr. Build. Mater.* **2021**, *318*, 125870.

32. Cavusoglu, I.; Yilmaz, E.; Yilmaz, A.O. Sodium silicate effect on setting properties, strength behavior and microstructure of cemented coal fly ash backfill. *Power Technol.* **2021**, *384*, 17–28. [CrossRef]

33. Libos, I.L.S.; Cui, L.; Liu, X. Effect of curing temperature on time-dependent shear behavior and properties of polypropylene fiber-reinforced cemented paste backfill. *Constr. Build. Mater.* **2021**, *311*, 125302. [CrossRef]

34. Ran, H.; Guo, Y.; Feng, G.; Qi, T.; Du, X. Creep properties and resistivity-ultrasonic-AE responses of cemented gangue backfill column under high-stress area. *Int. J. Min. Sci. Technol.* **2021**, *31*, 401–412. [CrossRef]

35. Hou, Y.; Yin, S.; Chen, X.; Zhang, M.; Yang, S. Study on characteristic stress and energy damage evolution mechanism of cemented tailings backfill under uniaxial compression. *Constr. Build. Mater.* **2021**, *301*, 124333. [CrossRef]

36. Yin, S.; Hou, Y.; Chen, X.; Zhang, M. Mechanical, flowing and microstructural properties of cemented sulfur tailings backfill: Effects of fiber lengths and dosage. *Constr. Build. Mater.* **2021**, *309*, 125058. [CrossRef]

37. Qiu, H.; Zhang, F.; Liu, L.; Huan, C.; Hou, D.; Kang, W. Experimental study on acoustic emission characteristics of cemented rock-tailings backfill. *Constr. Build. Mater.* **2021**, *315*, 125278. [CrossRef]

38. Xin, L. Meso-scale modeling of the influence of waste rock content on mechanical behavior of cemented tailings backfill. *Constr. Build. Mater.* **2021**, *307*, 124473. [CrossRef]

39. Zhao, K.; Huang, M.; Zhou, Y.; Yan, Y.; Wan, W.; Ning, F.; He, Z.; Wang, J. Synergistic deformation in a combination of cemented paste backfill and rocks. *Constr. Build. Mater.* **2022**, *317*, 125943. [CrossRef]

40. Liu, H.F.; Zhang, J.X.; Li, B.Y.; Zhou, N.; Li, D.Q.; Zhang, L.B.; Xiao, X. Long term leaching behavior of arsenic from cemented paste backfill made of construction and demolition waste: Experimental and numerical simulation studies. *J. Hazard. Mater.* **2021**, *416*, 125813. [PubMed]

41. Liu, L.; Fang, Z.Y.; Wu, Y.P.; Lai, X.P.; Wang, P.; Song, K.-I. Experimental investigation of solid-liquid two-phase flow in cemented rock-tailings backfill using Electrical Resistance Tomography. *Constr. Build. Mater.* **2018**, *175*, 267–276. [CrossRef]

42. Guicheng, H.; Shenglong, L.; Bingxiang, H.; Zhijun, Z.; Dexin, D. Reasonable matching for cemented waste rock backfill and sand shale. *J. Min. Saf. Eng.* **2017**, *34*, 371–376.

43. Yuye, T.; Xin, Y.; Weidong, S.; Haiping, W.; Shuai, C. Experimental study on combined pressure-bearing mechanism of filling body and surrounding rock. *J. Min. Saf. Eng.* **2018**, *35*, 1071–1076.

44. Wang, J.; Fu, J.X.; Song, W.D.; Zhang, Y.F.; Wang, Y. Mechanical behavior, acoustic emission properties and damage evolution of cemented paste backfill considering structural feature. *Constr. Build. Mater.* **2020**, *261*, 119958. [CrossRef]

45. Wang, J.; Fu, J.X.; Song, W.D.; Zhang, Y.F. Mechanical properties, damage evolution, and constitutive model of rock-encased backfill under uniaxial compression. *Constr. Build. Mater.* **2021**, *285*, 122898. [CrossRef]

46. Fu, J.X.; Wang, J.; Song, W.D. Damage constitutive model and strength criterion of cemented paste backfill based on layered effect considerations. *J. Mater. Res. Technol.* **2020**, *9*, 6073–6084. [CrossRef]

47. Liu, W.Z.; Chen, J.T.; Guo, Z.P.; Yang, H.Z.; Xie, W.W.; Zhang, Y.D. Mechanical properties and damage evolution of cemented coal gangue-fly ash backfill under uniaxial compression: Effects of different curing temperatures. *Constr. Build. Mater.* **2021**, *305*, 124820. [CrossRef]

48. Hou, J.F.; Guo, Z.P.; Li, J.B.; Zhao, L.J. Study on triaxial creep test and theoretical model of cemented gangue fly ash backfill under seepage-stress coupling. *Constr. Build. Mater.* **2021**, *273*, 121722. [CrossRef]

49. Lin, Q.B.; Cao, P.; Mao, S.Y.; Ou, C.J.; Cao, R.H. Fatigue behaviour and constitutive model of yellow sandstone containing pre-existing surface crack under uniaxial cyclic loading. *Theor. Appl. Fract. Mech.* **2020**, *109*, 102776. [CrossRef]
50. Ma, Q.; Tan, Y.L.; Liu, X.S.; Gu, Q.H.; Li, X.B. Effect of coal thicknesses on energy evolution characteristics of roof rock-coal-floor rock sandwich composite structure and its damage constitutive model. *Compos. Part B Eng.* **2020**, *198*, 108086. [CrossRef]
51. Hou, Z.K.; Gutierrez, M.; Ma, S.Q.; Almrabat, A.; Yang, C.H. Mechanical Behavior of Shale at Different Strain Rates. *Rock Mech. Rock Eng.* **2019**, *52*, 3531–3544. [CrossRef]
52. Jia, Z.Q.; Li, C.B.; Zhang, R.; Wang, M.; Gao, M.Z.; Zhang, Z.T.; Zhang, Z.P.; Ren, L.; Xie, J. Energy Evolution of Coal at Different Depths Under Unloading Conditions. *Rock Mech. Rock Eng.* **2019**, *52*, 4637–4649. [CrossRef]
53. Liu, B.; Huang, J.; Wang, Z.; Liu, L. Study on damage evolution and acoustic emission character of coal-rock under uniaxial compression. *Chin. J. Rock Mech. Eng.* **2009**, *28* (Suppl. 1), 3234–3238.
54. Barile, C.; Casavola, C.; Pappalettera, G.; Vimalathithan, P.K. Damage characterization in composite materials using acoustic emission signal-based and parameter-based data. *Compos. Part B Eng.* **2019**, *178*, 107469. [CrossRef]
55. Liu, X.S.; Tan, Y.L.; Ning, J.G.; Lu, Y.W.; Gu, Q.H. Mechanical properties and damage constitutive model of coal in coal-rock combined body. *Int. J. Rock Mech. Min. Sci.* **2018**, *110*, 140–150. [CrossRef]